

DOI: 10.1002/sml.200600595

# Nonaligned Carbon Nanotubes Anchored on Porous Alumina: Formation, Process Modeling, Gas-Phase Analysis, and Field-Emission Properties

Dmitry Lysenkov, Jörg Engstler, Arti Dangwal, Alexander Popp, Günter Müller,\* Jörg J. Schneider,\* Vinod M. Janardhanan, Olaf Deutschmann,\* Peter Strauch, Volker Ebert,\* and Jürgen Wolfrum

**We** have developed a chemical vapor deposition (CVD) process for the catalytic growth of carbon nanotubes (CNTs), anchored in a comose-type structure on top of porous alumina substrates. The mass-flow conditions of precursor and carrier gases and temperature distributions in the CVD reactor were studied by transient computational fluid dynamic simulation. Molecular-beam quadrupole mass spectroscopy (MB-QMS) has been used to analyze the gas phase during ferrocene CVD under reaction conditions (1073 K) in the boundary layer near the substrate. Field-emission (FE) properties of the nonaligned CNTs were measured for various coverages and pore diameters of the alumina. Samples with more dense CNT populations provided emitter-number densities up to  $48000\text{ cm}^{-2}$  at an electric field of  $6\text{ V}\mu\text{m}^{-1}$ . Samples with fewer but well-anchored CNTs in 22-nm pores yielded the highest current densities. Up to  $83\text{ mA cm}^{-2}$  at  $7\text{ V}\mu\text{m}^{-1}$  in dc mode and more than  $200\text{ mA cm}^{-2}$  at  $11\text{ V}\mu\text{m}^{-1}$  in pulsed diode operation have been achieved from a cathode size of  $24\text{ mm}^2$ .

## Keywords:

- alumina
- carbon nanotubes
- CVD
- field emission
- process simulation

[\*] Dr. D. Lysenkov, A. Dangwal, Prof. Dr. G. Müller  
Bergische Universität Wuppertal, Fachbereich C Abt. Physik  
Gaußstr. 20, 42097 Wuppertal (Germany)

Fax: (+49) 202-439-2811

E-mail: mueller@venus.physik.uni-wuppertal.de

Dr. J. Engstler, A. Popp, Prof. Dr. J. J. Schneider

Darmstadt University of Technology

Eduard-Zintl Institut für Anorganische und Physikalische Chemie

Petersenstr. 18, 64287 Darmstadt (Germany)

Fax: (+49) 6151-16-3470

E-mail: joerg.schneider@ac.chemie.tu-darmstadt.de

V. M. Janardhanan, Prof. Dr. O. Deutschmann

Universität Karlsruhe (TH)

Institut für Technische Chemie und Polymerchemie

Engesserstr. 20, 76131 Karlsruhe (Germany)

Fax: (+49) 721-608-4805

E-mail: deutschmann@ict.uni-karlsruhe.de

P. Strauch, Dr. V. Ebert, Prof. Dr. J. Wolfrum

Universität Heidelberg, Institut für Physikalische Chemie

Im Neuenheimer Feld 253, 69120 Heidelberg (Germany)

Fax: (+49) 622-154-5050

E-mail: volker.ebert@urz.uni-heidelberg.de

## 1. Introduction

Cold field-emission (FE) cathodes are considered as one of the most promising applications of CNTs because of their quasi-one-dimensional structure with naturally high aspect ratios. They can provide field-enhancement factors above 1000 and thus threshold fields in the  $\text{V}\mu\text{m}^{-1}$  range.<sup>[1-4]</sup> Current limits up to  $2\text{ }\mu\text{A}$  for single-wall<sup>[5]</sup> and  $20\text{ }\mu\text{A}$  for multi-walled CNTs<sup>[6]</sup> have been obtained even at moderately high vacuum conditions under which usual FE metal tips begin to deteriorate. Applications such as flat-panel displays<sup>[7]</sup> or X-ray tubes<sup>[8]</sup> and microwave amplifiers<sup>[9]</sup> require large emitter numbers with uniform and stable FE properties.<sup>[3]</sup> Since densely grown CNTs show mutual shielding effects,<sup>[10]</sup> a selective growth of CNTs is most desirable for controllable FE devices.<sup>[11]</sup> As an alternative approach, CNT bundles with a low degree of individual CNT ordering have been pursued and are promising with respect to the achieved emitter numbers<sup>[12]</sup> and current densities.<sup>[13]</sup>

The chemical vapor deposition (CVD) approach to the synthesis of CNTs allows the use of a wide range of precursor molecules to form different CNT morphologies.<sup>[14–20]</sup> Metal-catalyzed CNT formation proceeds either via the vapor–liquid–solid (VLS) mechanism<sup>[21]</sup> or by cap growth on top of the catalyst metal particles (Yarmulke mechanism).<sup>[22]</sup> In the latter case the catalyst particles can be found at the tube bottom, in the former case at the tube end. Catalyst particles can be introduced either 1) onto the substrate by a preimpregnation step prior to CNT formation, 2) parallel with the precursor gas but generated from a different precursor, or 3) chemically bound to the carbon source from which the CNTs are formed. The latter technique uses the single-source-precursor concept for CNT formation. [Fe(CO)<sub>5</sub>],<sup>[23]</sup> Fe(phtalocyanine),<sup>[24,25]</sup> ferritin,<sup>[26]</sup> or metalloenes such as ferrocene<sup>[2,16]</sup> are prominent examples of precursors used for this technique.

We report here on an integrated approach to study the formation, CVD process modeling, gas-phase species analysis, and FE properties of CNTs anchored on porous alumina substrates. Our earlier synthetic studies with regular CNT filling of all pores of alumina templates showed only weak FE at the edges due to strong mutual shielding of the emitters.<sup>[27,28]</sup> Therefore we developed a new approach to isolate emitters on a statistical basis on alumina substrates with varying pore diameters.<sup>[29]</sup> Important parameters in the gas-phase reactivity of ferrocene and reactive species formed under reaction conditions leading to CNT growth were identified. We will also show that nonaligned, but well-anchored CNTs yield favorable FE properties for high-current applications when attached to porous alumina.

## 2. Results and Discussion

### 2.1. CNT Synthesis

We used ferrocene, [(C<sub>5</sub>H<sub>5</sub>)<sub>2</sub>Fe], as a single-source precursor for CNT formation. No other process gas was added. The carbon source and catalyst was always supplied under constant ratio. Our earlier CVD experiments with ferrocene as a precursor using bare porous alumina membranes with a complete open-pore structure had already yielded promising FE characteristics. These studies showed that CNTs deposited on porous alumina have definite advantages in the resulting FE performance over other substrate systems. We attribute this to the formation of isolated, scattered CNTs on the surface of the porous membranes.<sup>[27,28]</sup> Due to the promising FE characteristics of this material, it would be desirable to enhance CNT growth on the substrate to further increase the individual emitter density. We therefore decorated the surface of porous alumina membranes with isolated, randomly distributed alumina islands. These isolated alumina islands on the surface of the porous alumina substrate membrane were deposited by CVD using volatile aluminum tris(*sec*-butoxide) **1** as the precursor for alumina particle deposition.<sup>[18]</sup> Deposition of **1** onto the surface of the porous alumina substrates (various different pore diameters) results

in the formation of islands of irregularly arranged alumina dots on the porous alumina substrate surface (Figure 1).

Our homemade porous alumina templates provide smaller pore diameters compared to the commercial ones

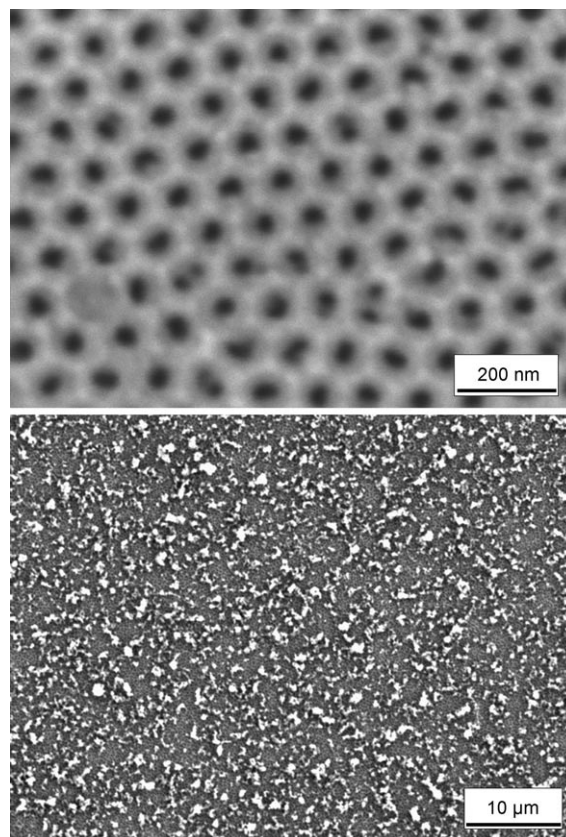


**Figure 1.** Top: Native porous alumina substrate with 60-nm pore-diameter. Bottom: Alumina islands formed via CVD using Al(*sec*-butoxide)<sub>3</sub> on the surface of a porous Anodisc template (pore diameter 200 nm).

(variable between 20–70 nm compared to 200 nm).<sup>[30]</sup> The density of the alumina islands on the various porous substrates could be steered by the amount of precursor used. Their size and irregular shape varied in the range of several-hundred nanometers up to a few micrometers. The islands overgrow and cover parts of the porous alumina template structure. These isolated alumina islands serve as growth sites for the CNT growth process using ferrocene. CVD growth of CNTs on such substrates (Ar carrier gas;  $T_{\text{depos}} = 1123$  K) did indeed yield CNTs that were randomly, but homogeneously distributed across the substrate surface. The CNTs are anchored on the deposited alumina islands resulting in a comose-like (tufted) structure as revealed by scanning electron microscopy (SEM, Figure 2). In addition to this finding, individual CNT structures were also deposited directly on top of the porous alumina substrate. These are either directly anchored onto the alumina surface or even fixed in the pores of the substrate (Figure 2, bottom). We speculate that this special type of CNT/substrate morphology results in a stabilizing effect towards the individual FE

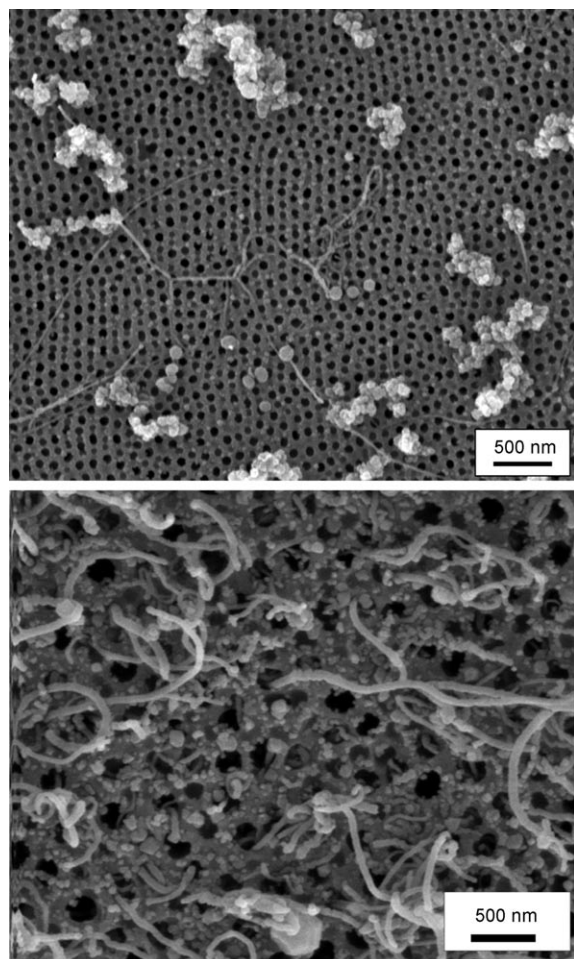


**Figure 2.** SEM of the alumina/CNT composite structure. Top: Isolated CNTs growing on top of the alumina islands, which were predeposited by CVD onto a porous alumina surface (template pore diameter 40 nm). Bottom: Magnified view of CNTs anchored on top or inside the pores of the porous alumina substrate.

properties of the alumina/CNT composite material (see Chapter 2.4).

High-resolution transmission electron microscopy (HRTEM) identifies the tube morphology on top of the alumina surface as multi-walled (MW) CNTs with a bamboo-type structure (Figure 3, upper to lower right). Samples of isolated CNTs for TEM were obtained by detaching the CNT loaded alumina islands from the substrate surface mechanically. Still some CNTs stay securely anchored to the alumina particle surface, manifesting the robustness of the alumina particle/CNT composite structure (Figure 3 upper left). These CNTs show an irregular shape with a diameter between 10 and 20 nm. Their inner hollow is irregularly filled with iron rods of up to 100 nm in length. Iron-filled CNTs were found by us and others when using ferrocene as a precursor.<sup>[15–17]</sup>

An important question for the performance in FE experiments is how good electrical conductivity throughout the dielectric alumina template material can be realized with this arrangement? The first step in our synthesis process is the deposition of isolated alumina islands on top of

the porous template by a CVD process using a volatile organoaluminum compound. After this, the CNT structures are formed and anchored to these islands via CVD using ferrocene. When this formation process occurs, the formation of an additional carbon tube structure inside the porous alumina substrate takes place simultaneously.<sup>[17,30]</sup> The diameter of these inner CNTs corresponds exactly to the pore diameter of the alumina template. The deposition of this inner carbon-tube structure ensures that the whole composite structure, composed of alumina and embedded CNTs, is electrically conducting throughout the whole sample, from its bottom side up to the tips of the MWCNTs, which grew on the alumina islands. The alumina/CNT structure (Figure 4) used in the FE studies (Chapter 2.4) has a nominal thickness of up to 60  $\mu\text{m}$ .

## 2.2. Theoretical CVD Process Simulation Studies

### 2.2.1. CFD Study

The mass-flow conditions of precursors, carrier gases, and temperature distributions in the CVD reactor were systematically studied by transient computational fluid dynamics (CFD) simulations. The simulations are carried out using the commercial CFD code FLUENT,<sup>[31]</sup> which solves the transient Navier–Stokes equations coupled with transport equations for temperature and each chemical species. The simulations assume that all of the ferrocene evaporates in 2 min; ferrocene enters the reactor through the second inlet (see Experimental Section for more information on the setup). The properties of the mixed species are evaluated using mixing law. The mass flow of ferrocene and the transient time steps are adjusted using user-defined functions (UDFs).<sup>[31]</sup> The evolution of the temperature distribution is shown in Figure 5.

It is quite evident from the plot that the temperature over the substrate reaches a steady state at  $\approx 90$  s. The reactor is divided into three zones with zone 1 maintained at 623 K and zones 2 and 3 at 1123 K. Figure 6 shows the evolution of precursor concentration and temperature over the substrate. During the initial stages the temperature and precursor concentrations are not uniform over the substrate. However at nearly 100 s, both temperature and precursor composition achieve uniform values over the substrate. It should be noted that for the CFD simulations, precursor decomposition is not considered. Such calculations using one-dimensional plug-flow simulations are explained in the following section.

### 2.2.2. Kinetic Study

Plug-flow reactor models are well suited for small-diameter reactors for which the axial diffusion can safely be neglected and infinite mixing in the radial direction can be assumed. Under these conditions, plug-flow reactor equations can be solved using the software DETCHEMPLUG<sup>[32]</sup> to derive the species profiles during the gas-phase decomposition of ferrocene. The governing equations for the plug-flow

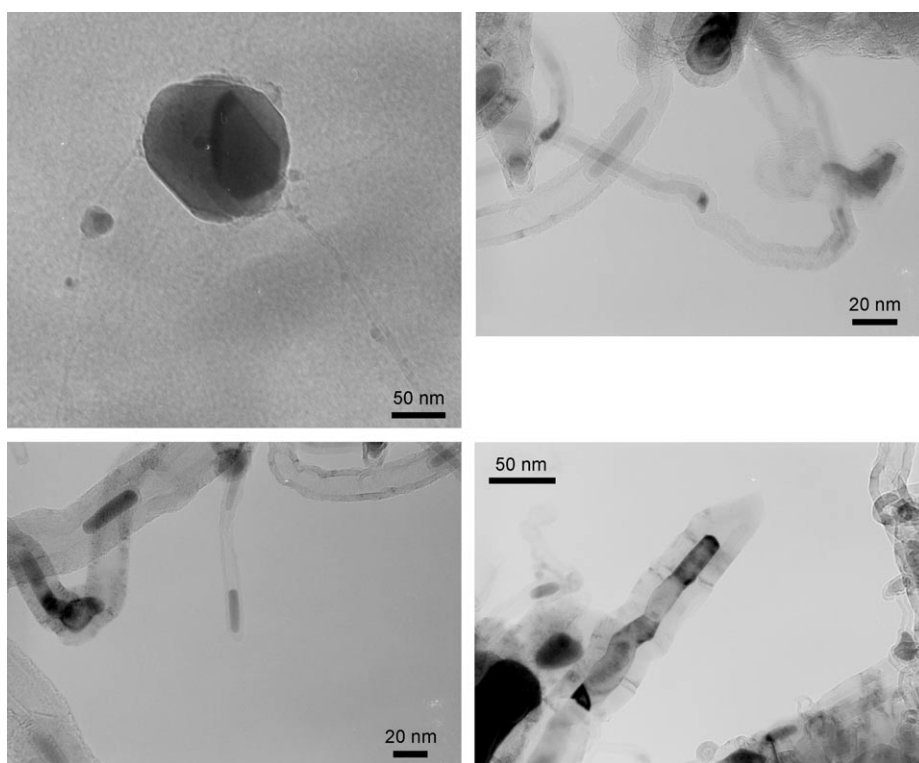


**Figure 3.** Upper left: HRTEM image of an isolated alumina particle with anchored CNTs on its surface obtained after detachment of the alumina particles from the porous alumina substrate surface. Others: HRTEM images of multi-walled CNTs harvested from the alumina particle surface.

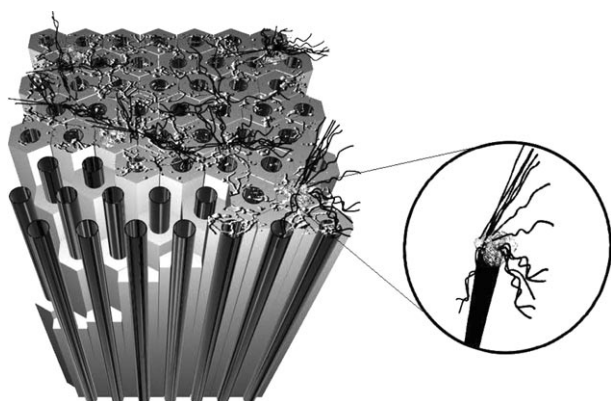


**Figure 4.** Structure model showing the CNT comose arrangement on top of the alumina template. The inset shows the disordered, alumina-embedded growth of SWCNTs on top of an alumina island. Within the porous alumina substrate carbon filaments are formed due to the straight pore channels of the template.

reactor are one-dimensional in nature with axial position as the independent variable. The chemistry model is implemented using an elementary-step gas-phase kinetics consisting of 2653 reactions among 299 species. The mechanism is basically derived from different sources: Ferrocene decomposition reaction steps are taken from Hirasawa et al.<sup>[53]</sup> In this mechanism, ferrocene decomposition is described by a five-step reaction mechanism and the formation of aromatics is described by irreversible kinetics. However, the mechanism does not account for any agglomeration of Fe. Re-

maintaining steps in the mechanism are taken from Sheng and Dean.<sup>[34]</sup> This mechanism includes kinetics for higher-molecular-weight growth especially involving propargyl radical pathways, and explicit inclusion of certain  $C_6$  hydrocarbon species, including *n*-hexane, cyclohexane, and 2,3-dimethylbutane.

For the simulations, 5% ferrocene diluted in Ar is assumed to enter the reactor at  $0.3 \text{ ms}^{-1}$ , and the calculations are carried out under steady-state and isothermal conditions. The simulation results for the major species formed during gas-phase decomposition are shown in Figure 7. Other than the formation of Fe during the decomposition of ferrocene,  $H_2$ ,  $C_{10}H_8$ ,  $C_{12}H_8$ ,  $C_6H_6$ ,  $CH_4$ , and  $C_2H_4$  were found to be the major species. Other than these, traces of other hydrocarbons

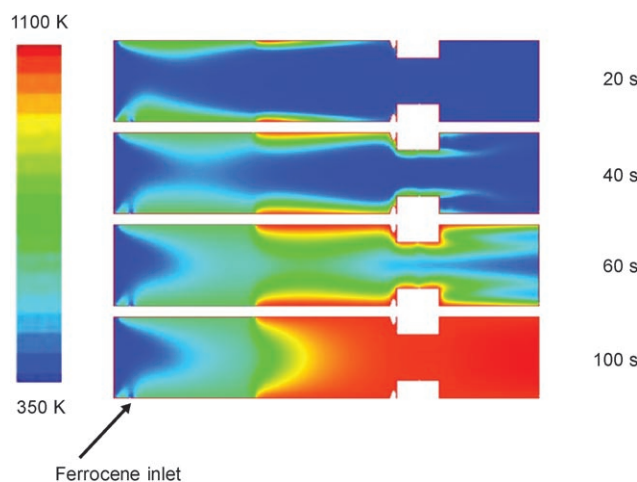


**Figure 5.** Contour plots of temperature for the transient reactor simulation

are also formed during the decomposition process. However, due to their minute presence they are not shown in Figure 7.

Simulations were further carried out for varying reactor temperatures to elucidate the dependence of reaction products on temperature. As evident from Figure 8, ferrocene starts to decompose at  $\approx 975 \text{ K}$ . The concentration of all of the products increases with increasing temperature. However, naphthalene ( $C_{10}H_8$ ) starts to further decompose at  $1073 \text{ K}$ .

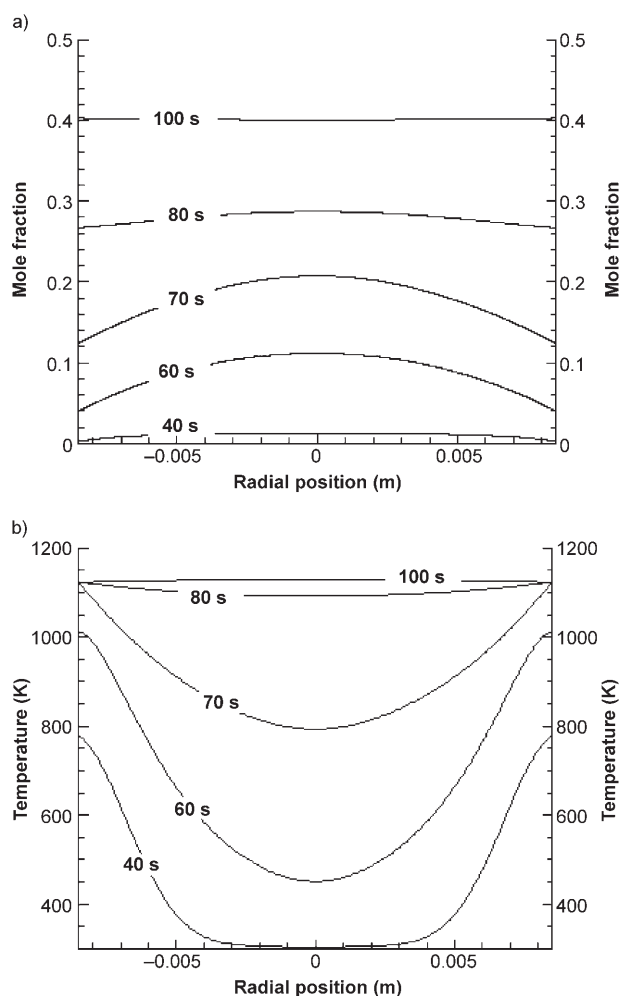


Figure 6. Evolution of a) temperature and b) concentration over the substrate.

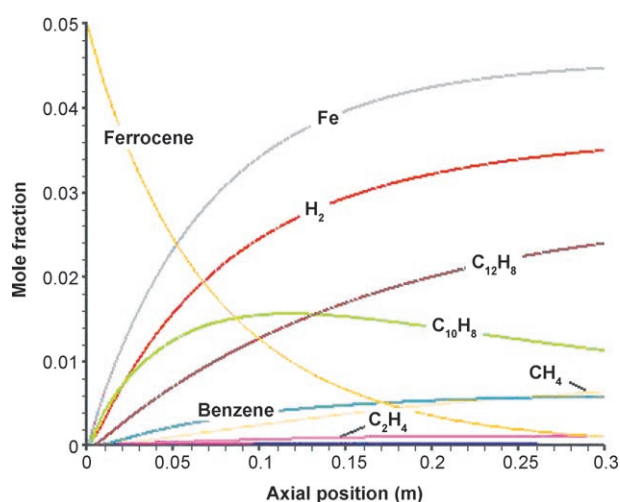


Figure 7. Species profiles as a function of reactor length during the gas-phase decomposition of ferrocene at 1123 K.

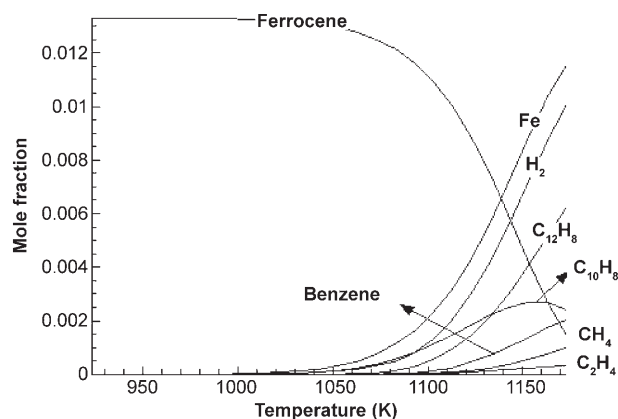


Figure 8. Temperature-dependent species profiles measured in the substrate boundary layer during the gas-phase decomposition of ferrocene using MB-QMS.

### 2.3. Experimental Gas-Phase Studies

One intention of the gas-phase study was to identify key reactive and stable species during CNT formation, first, for process-control purposes in the CNT formation process using, for example, optical analytical techniques, and second, to provide feedback to the modelling studies of the gas phase chemistry. Thus we acquired temperature-resolved mass spectra between 1 and 300 amu during the ferrocene-based CVD process on crystalline sapphire and commercial Anodisc substrates.

Using low-pressure CVD, dense deposits of CNTs (Figure 9) could be successfully grown from the ferrocene precursor on the sapphire substrate in the titanium reactor setup described in the Experimental Section. The boundary layer above the substrate where the CNTs were formed was analyzed by MB-QMS. This allows an in situ characterization of gas-phase species formed from the precursor molecule under the real reaction conditions that lead to CNT growth on the substrate. Despite using a concentric flow configuration, which was expected to lead to stagnation flow, we found an asymmetric carbon distribution on the substrate at low-temperature conditions. This is attributed to the off-axial removal of the reactor gases in our specific reactor configuration.

In order to separate the reaction products of the ferrocene decomposition/CNT formation from fragmentation products by the electron-beam ionization, we recorded temperature-dependent mass spectra at 373, 773, 873, and 973 K and compared the evolution of the spectra with regard to the ferrocene stability limit near 823 K. Initially higher temperatures (on the order of 1173 K) were used, but the rapid deposition of conducting carbon deposits onto the boron nitride heaters changed the resistance of the heater thus limiting the maximum temperature to 1043 K. Even though most of the ferrocene is not decomposed at these rather low temperatures, it was possible (owing to the sensitivity of the MB-QMS technique) to detect numerous ferrocene and hydrocarbon fragments and to monitor the onset of ferrocene decomposition and CNT formation by the strong rise in

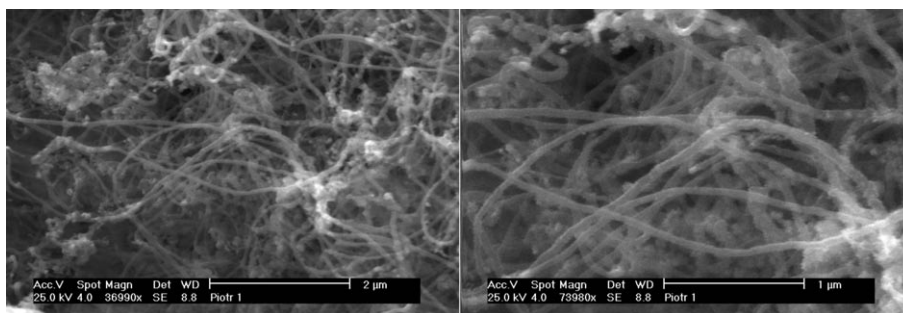


**Figure 9.** Carbon nanotubes deposited onto crystalline sapphire substrates in the molecular beam reactor.

some reactive intermediate species. Comparing the mass spectra from ferrocene CVD with published fragmentation spectra<sup>[35]</sup> we isolated species that were either not expected in the ferrocene fragmentation spectrum, or that showed a pronounced signal increase above the ferrocene dissociation temperature range around 823 K. Fluctuations in the ferrocene concentration were suppressed by normalizing all peaks to  $m/z = 186$ . Table 1 lists the selected fragments that fulfill these conditions.

**Table 1.** Selected reactive species detected in ferrocene CVD using MB-QMS.

Species	$m/z$	FeCp <sub>2</sub> fragmentation product	Model species
H <sub>2</sub>	2	–	yes
C <sub>3</sub> H <sub>5</sub> , C <sub>3</sub> H <sub>7</sub>	41, 43	–	–
FeH	57	–	–
FeCH <sub>x</sub> ( $x = 1, 2, 3$ )	69, 70, 71	–	–
C <sub>3</sub> H <sub>3</sub>	39	yes	–
Fe	56	yes	yes
FeCp	121	yes	yes
C <sub>10</sub> H <sub>8</sub>	128	yes	yes

Detected species that were not expected from the ferrocene fragmentation spectrum were H<sub>2</sub>, C<sub>3</sub>H<sub>x</sub> ( $m/z = 41, 43$ ;  $x = 5, 7$ ), FeH ( $m/z = 57$ ) and FeCH<sub>x</sub> ( $m/z = 69, 70, 71$ ;  $x = 1, 2, 3$ ). Out of these the strongest signal with the strongest temperature dependence is found to be H<sub>2</sub>, which was completely absent below 873 K. Additionally, decomposition/CNT formation product candidates that are fragmentation products, but which show a pronounced signal variation above the ferrocene stability limit were: C<sub>3</sub>H<sub>3</sub> ( $m/z = 39$ ), Fe (56), FeCp (121), and C<sub>10</sub>H<sub>8</sub> (128). Only small changes were found on the fragmentation peaks of FeC<sub>2</sub>H<sub>x</sub> and FeC<sub>3</sub>H<sub>x</sub>. FeC<sub>4</sub>H<sub>x</sub>, as well as FeC<sub>y</sub>H<sub>x</sub> with  $y \geq 6$  were below the detection limit. Comparing the qualitative behavior of our temperature dependence (Figure 10) with the model prediction (Figure 8), we could verify the same strong temperature dependence for all molecules, which is expected to rise at rather low temperatures as there are such products as H<sub>2</sub>, Fe, and C<sub>10</sub>H<sub>8</sub>. Other predicted products such as CH<sub>4</sub>, C<sub>2</sub>H<sub>4</sub>, benzene, and C<sub>12</sub>H<sub>8</sub> could not be detected as all of

these species appear relatively late at rather high temperatures, which were not used in our experiment. In addition, CH<sub>4</sub> and C<sub>2</sub>H<sub>4</sub> QMS-signals suffered from H<sub>2</sub>O and N<sub>2</sub> interference. Future work will therefore focus on the detection of CH<sub>4</sub> and C<sub>2</sub>H<sub>4</sub> by in situ laser absorption spectroscopy, which we previously reported with up to sub-ppm detection for CH<sub>4</sub>,<sup>[36,37]</sup> while a C<sub>2</sub>H<sub>4</sub> laser sensor was demonstrated by Hanson et al.<sup>[38]</sup> Furthermore the substrate heater is currently being modified to enable higher temperatures up to 1223 K and to incorporate the absolute quantification of the QMS signals using literature data of ionization probabilities according the procedure of Biordi.<sup>[39]</sup>

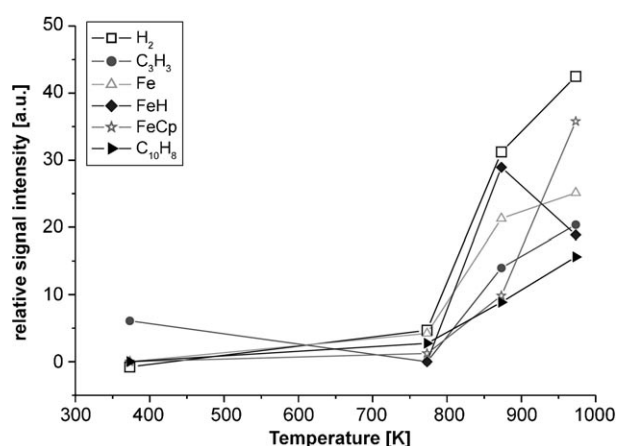


**Figure 10.** Temperature dependence of selected QMS signals during ferrocene CVD. All signals except H<sub>2</sub> are corrected for baseline contribution due to ferrocene fragmentation.

#### 2.4. Field-Emission Studies

It is well known that CNT cathodes on porous alumina substrates have a limited size, irregular shape, and finite curvature due to the brittleness and unavoidable shrinkage of the hydrophilic alumina during CVD processes with thermal cycling up to 800 °C. Therefore, we have controlled the resulting shape and flatness of the CNT cathodes by means of an optical profilometer (FRT MicroProf), which provides nondestructive measurements with micrometer resolution. Measured profiles of typical samples of about 20 mm<sup>2</sup> size with concave or convex curvature are given in Figure 11. The concave sample shows a nearly rhombohedral shape with sharp edges exposed up to 120 μm above the center region, which reveals the substrate thickness to be about 100 μm. In contrast, the more rectangular convex sample shows a height difference up to 100 μm with maxima at the left edge and central ridge structure.

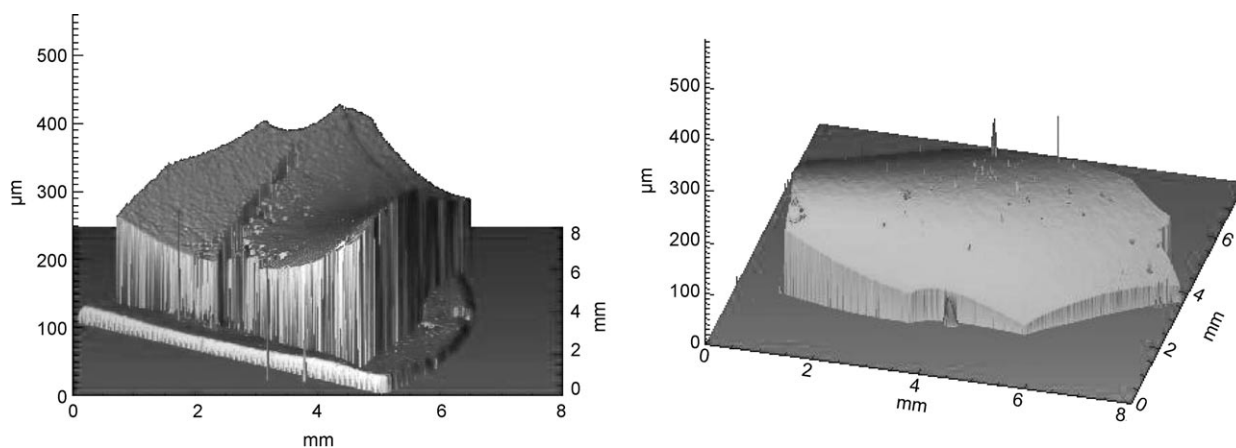


Figure 11. 3D profiles of CNT cathodes on porous alumina. Left: concave curvature (22.4 mm<sup>2</sup>); right: convex curvature (24 mm<sup>2</sup>). The height scale is magnified for better illustration.

Obviously, the curvature of the cathodes affects the FE measurements, especially in diode configuration. Since the adjustable electrode spacing between the sample and the phosphor screen ( $\Delta z$ ) in our integral current measurement system (with a luminescent screen (IMLS)<sup>[40]</sup>) is typically 300  $\mu\text{m}$ , a non-flat field up to about 30% has to be taken into account, despite of the effective electric-field calibration by means of  $U(z)$  plots.<sup>[41]</sup> Accordingly, the IMLS images of the two curved samples (Figure 12) yield the strongest FE in those areas that are exposed to the highest field. This edge emission has often hindered the full exploitation of our CNT cathodes. Emitter number densities  $N(E)$  of more than 7000  $\text{cm}^{-2}$  at 5(7)  $\text{V}\mu\text{m}^{-1}$  and 3500  $\text{cm}^{-2}$  at 3  $\text{V}\mu\text{m}^{-1}$  result from these images with 20  $\mu\text{m}$  resolution, respectively. The corresponding current densities  $j$  for these images are 12 and 83  $\text{mA}\text{cm}^{-2}$  in dc operation. In accordance with the non-flat field and the expected spread of the CNT lengths on porous alumina, the integrally measured FE current of the CNT cathodes in Figure 13 shows a non-linear Fowler–Nordheim (FN) dependence, which is also influenced by processing effects.

During the initial increase of the field four regimes with different linear slopes can be extracted, which correspond to field-enhancement factors  $\beta$  between 700 and 2000 for an assumed work function  $\Phi = 4.9$  eV.<sup>[42]</sup> The FN plot for the

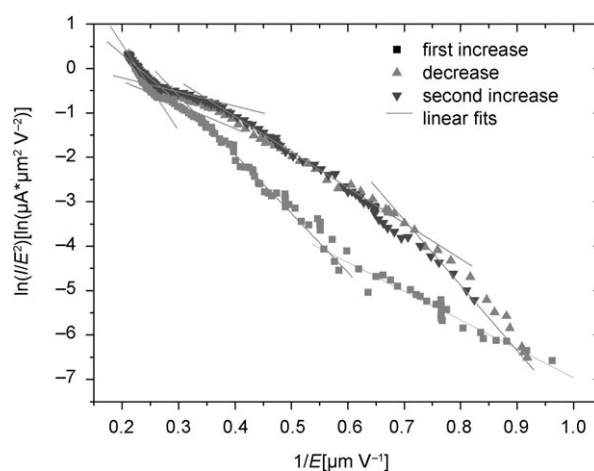


Figure 13. FN plot of the integral current measured for a typical CNT cathode on porous alumina showing various slopes due to the superposition of emitters and processing effects.

field decrease and second increase becomes more reproducible at higher current levels but still shows various slopes, that is,  $\beta$  values of 1100, 2100, 1200, and 800. Such slope changes are usually caused by the superposition of many CNT emitters with different FN parameters, which have been found by other authors as well.<sup>[43]</sup> It is remarkable that our samples with non-aligned CNTs provide at least a few emitters with high  $\beta$  values above 2000 resulting in low onset fields  $E_{\text{on}}$  for 1 nA of about 1  $\text{V}\mu\text{m}^{-1}$ . The observed irreversible changes of the integral  $I$ - $V$  curves reflect the local activation and deactivation of emitters, both of which have been demonstrated by the analysis of consecutive IMLS images.<sup>[29,44]</sup> After dc process-

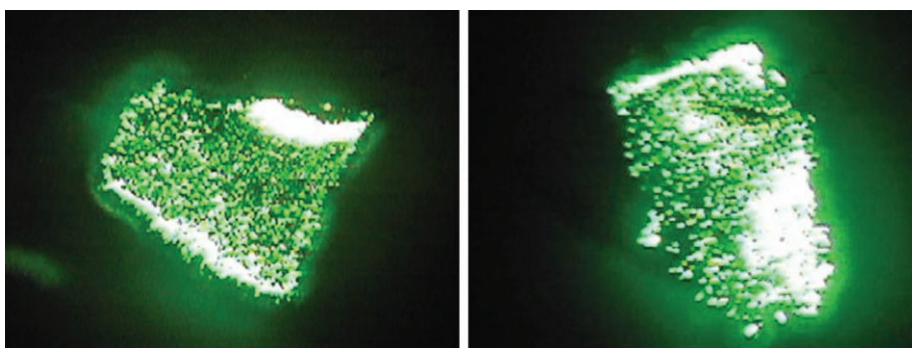


Figure 12. IMLS images of the same CNT cathodes as in Figure 11. Left:  $\Delta z = 200$   $\mu\text{m}$  and  $U = 1090$  V,  $I = 2.7$  mA. Right: Comparison with a more flat cathode of 18.2 mm<sup>2</sup> size at  $\Delta z = 350$   $\mu\text{m}$ ,  $U = 1400$  V,  $I = 20$  mA.

ing times of some hours, the emission of the CNT cathodes usually becomes more stable and uniform at the expense of about 40% less current at a given field.<sup>[29]</sup>

The main result of the systematic variation of the fabrication parameters of the CNT cathodes is a strong correlation between the average alumina pore diameter and the processed integral current density  $j$ , as shown in Figure 14. While commercial Anopore substrates with 200 nm pores yield  $j$  values below  $1 \text{ mA cm}^{-2}$  at  $4 \text{ V } \mu\text{m}^{-1}$ ,  $j$  values up to four times higher have been achieved for CNTs grown on our alumina templates with pore diameters between 20 and 30 nm.<sup>[45]</sup> Considering the average diameter of 20 nm of our multi-walled CNTs, their improved anchoring within the pores is suggested as a most straightforward explanation for this improvement.

In order to exploit the full potential of our CNTs on porous alumina for FE applications, we have performed high-resolution regulated voltage scans  $U(x,y)$  for a given maximum current and local measurements of the FN parameters of single emitters by means of a field-emission scanning microscope (FESM).<sup>[40]</sup> Figure 15 shows typical  $U(x,y)$  results for CNT samples with 200 and 42 nm pore diameters, which obviously show a higher emitter number density  $N(E)$  for the case with larger pores. The  $N(E)$  values found in the FESM U-maps are above  $10000 \text{ cm}^{-2}$  at  $6 \text{ V } \mu\text{m}^{-1}$ , that is, slightly higher than those in the IMLS images because of voltage adaptation and higher spatial resolution of the tungsten tip anodes.

It is most remarkable that fewer emitters on smaller pore-diameter samples provide higher current densities, thus underlining the hypothesis of the improved anchoring

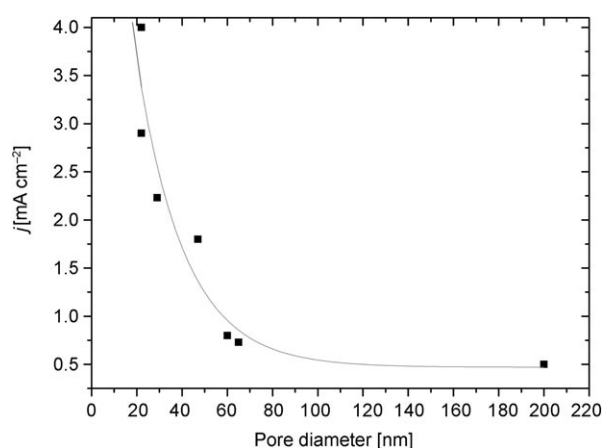


**Figure 14.** Influence of the pore diameter of the alumina on the integral current density from CNT cathodes achieved at an effective electric field of  $4 \text{ V } \mu\text{m}^{-1}$ .

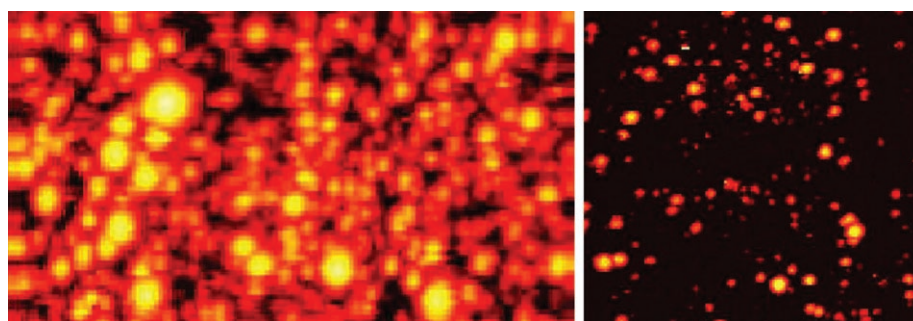


**Figure 15.** U maps (scan area  $1 \times 0.5 \text{ mm}^2$ ) of CNTs. Left: on 200-nm pores ( $W$  anode tip diameter =  $20 \text{ } \mu\text{m}$ ,  $\Delta z = 20 \text{ } \mu\text{m}$ ,  $I = 10 \text{ nA}$ ); right: on 42-nm pores ( $W$  anode tip diameter =  $12 \text{ } \mu\text{m}$ ,  $\Delta z = 14 \text{ } \mu\text{m}$ ,  $I = 1 \text{ nA}$ ). The resulting emitter number densities  $N(E)$  are  $60000 \text{ cm}^{-2}$  at  $8.8 \text{ V } \mu\text{m}^{-1}$  and  $24000 \text{ cm}^{-2}$  at  $12 \text{ V } \mu\text{m}^{-1}$ .

of CNTs in smaller alumina pores. Therefore, the FN parameters ( $\Phi = 4.9 \text{ eV}$ ) of randomly chosen emitters of both samples were compared (Figure 16). The emitters on 200-nm alumina pores provide a larger spread of  $\beta$  values and,

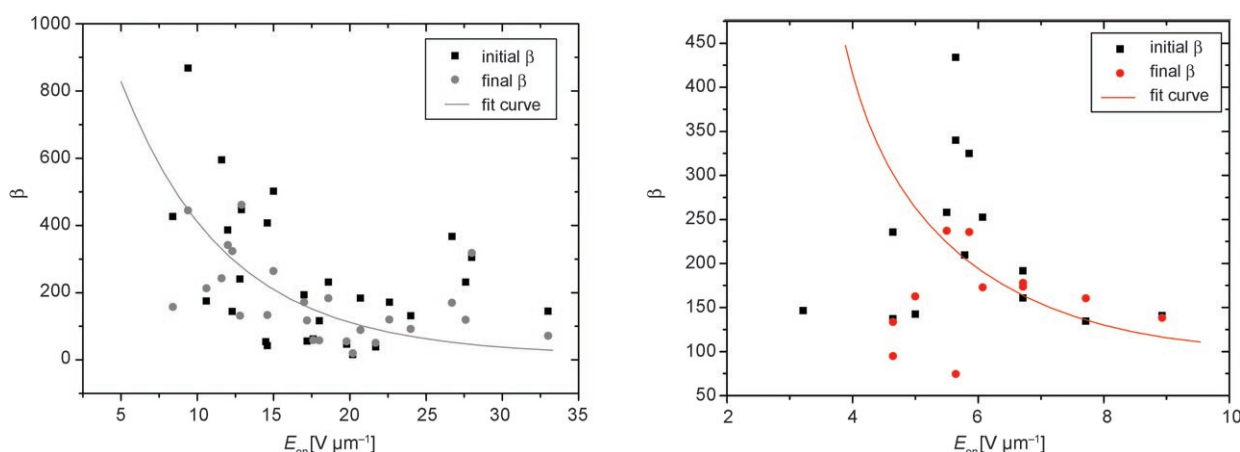


**Figure 16.** Comparison of the field enhancement factor  $\beta$  as a function of the onset field for 1 nA determined for 30 (20) randomly chosen emitters on the same CNT samples as in Figure 9, that is, left: 200 nm pores; right: 42 nm pores. Please note that some emitters were destroyed during the voltage cycles.

on average, higher  $E_{\text{on}}$  values (15–870 at 8–32.5  $\text{V}\mu\text{m}^{-1}$ ) than those on 42 nm pores (140–450 at 3–9  $\text{V}\mu\text{m}^{-1}$ ). This might be explained by the different growth conditions of the CNTs for constant ferrocene mass flow. In SEM images on large-pore samples, mostly short ( $<0.5\ \mu\text{m}$ ) and only a few longer CNTs ( $>2\ \mu\text{m}$ ) are visible, while on smaller pore samples less but more uniform CNTs are observed.<sup>[28,41,46]</sup> Beside the strong processing effects, the emitters on both samples show an inverse  $\beta(E_{\text{on}})$  correlation, as expected from FN theory.

For FE cathode applications the current-carrying capability of single CNTs is most interesting. Therefore, we have tried to reach the current limits of our MWCNTs by local FESM measurements with high resolution ( $<10\ \mu\text{m}$ ). Accordingly, the voltage was increased until strong current fluctuation or degradation occurred. On average the emitters on the 200 nm alumina pores provided much lower maximum currents  $I_{\text{max}}$  ( $\approx 2\ \mu\text{A}$ ) than those on 22-nm pores ( $\approx 9\ \mu\text{A}$ ), thus again confirming the hypothesis of improved CNT anchoring. The corresponding FN plots of the best emitters (8.6  $\mu\text{A}$  and 19.7  $\mu\text{A}$ , respectively) are shown in Figure 17. Assuming that only one MWCNT is involved, these  $I_{\text{max}}$  values are close to the highest reported in the literature.<sup>[5]</sup>

It is tempting to extrapolate maximum achievable dc current densities  $j$  above  $0.2\ \text{A}\text{cm}^{-2}$  for the best CNT samples at  $10\ \text{V}\mu\text{m}^{-1}$  by multiplying the average  $I_{\text{max}}$  and  $N(E)$  values as determined by the FESM. For real cathodes in the IMLS, however, such high  $j$  values can not be realized because of the high power load on the luminescent screen,

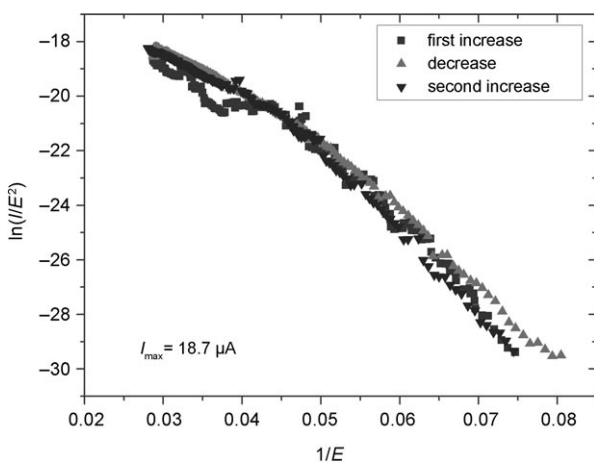


Figure 17. Locally measured FN plots and maximum currents  $I_{\text{max}}$  of the best CNT emitters on a) 200 nm and b) 22 nm alumina pores.

which leads to evaporation of the “phosphor” and damaging discharges.<sup>[44]</sup> Therefore, we have switched the measurements from dc to pulsed operation with duty cycles of at least 1:10 at the first evidence of “phosphor” traces (e.g., by mass spectrometry of corresponding gas species). Accordingly, high peak-current densities  $j_p$  up to  $45\ \text{mA}\text{cm}^{-2}$  at  $7.5\ \text{V}\mu\text{m}^{-1}$  for CNTs on 29-nm pores and more than  $0.2\ \text{A}\text{cm}^{-2}$  (only limited by the power supply) at  $11.5\ \text{V}\mu\text{m}^{-1}$  on 22-nm alumina pores have been achieved, as shown in Figure 18. It should be mentioned that the impres-

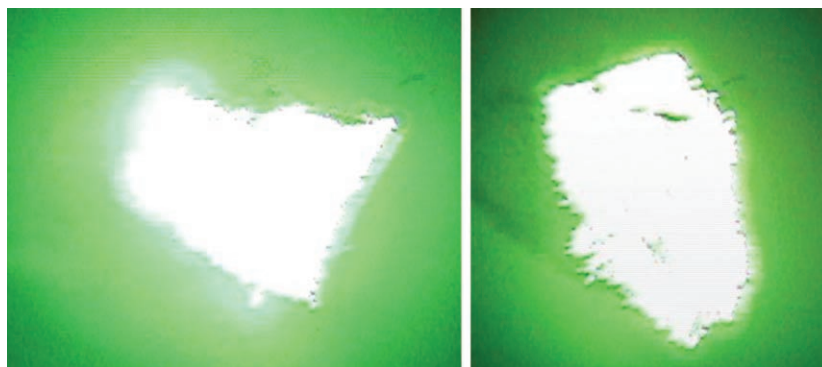


Figure 18. Pulsed-mode IMLS images of CNT samples. Left: on 29-nm pores (22.4  $\text{mm}^2$ ,  $U = 1500\ \text{V}$ ,  $\Delta z = 200\ \mu\text{m}$ ,  $I_p = 10\ \text{mA}$ ). Right: on 22-nm pores (24  $\text{mm}^2$ ,  $U = 2300\ \text{V}$ ,  $\Delta z = 200\ \mu\text{m}$ ,  $I_p = 50\ \text{mA}$ ). For the latter image a 20% transmission filter was used for protection of the CCD camera.

sion of much improved FE homogeneity is partially caused by the lateral light spread in the luminescent screen, which is useful for light-source applications.<sup>[41]</sup>

The FE performance of our best CNT samples on alumina with different pore diameters are summarized in Table 2. Obviously, these results confirm the correlation shown in Figure 18, now at higher electric fields in both dc and pulsed modes. Thus, the benefit of smaller pore size on high current densities is due to the improved anchoring of the CNTs. The comparably small dc  $j_{\text{max}}$  values of the samples with 65 and 60 nm pores were limited by rather inhomogeneous FE. The new record current density of  $0.2\ \text{A}\text{cm}^{-2}$  at  $11.5\ \text{V}\mu\text{m}^{-1}$  for the 24  $\text{mm}^2$  size cathode with 22-nm pores is close to the best values reported in the literature.<sup>[5]</sup>

### 3. Conclusions

By using an integrated experimental and theoretical approach we were able to optimize the field-emission properties of nonaligned CNTs on porous alumina substrates. Isolated CNTs were either anchored on top of alumina nucleation sites or in the pores of the substrate by thermal CVD. This ensures that the CNTs show a good intergrowth and mechanical stability with the substrate (comose-type structure) resulting in very good FE performance properties. With this selective growth approach we have bypassed mutual shielding effects typically observed for CNT arrays.<sup>[11]</sup> This is an important step towards controllable FE devices. For the first time, transient CFD simulations were

**Table 2.** Overview of the emitter-number densities  $N_{\max}$  and maximum dc and pulsed integral current densities  $j_{\max}$  achieved at the corresponding fields  $E_{\max}$  for the best CNT samples on alumina with different pore diameters.

Average pore diameter [nm]	Sample area [mm <sup>2</sup> ]	$N_{\max}$ [cm <sup>-2</sup> ]	dc (IMLS)		Pulsed (IMLS)		FESM	
			$j_{\max}$ [mAcm <sup>-2</sup> ]	$E_{\max}^{\text{eff[a]}}$ [V $\mu\text{m}^{-1}$ ]	$j_{\max}$ [mAcm <sup>-2</sup> ]	$E_{\max}$ [V $\mu\text{m}^{-1}$ ]	$N_{\max}$ [cm <sup>-2</sup> ]	E [V $\mu\text{m}^{-1}$ ]
200	24.7	7000	1.2	3	5.6	12.3	60000	8.8
65	13	1500	0.75	4.1	58	7.6	–	–
60	8	6000	0.8	4	–	–	62000	23
42	31	10000	32	7.2	–	–	24000	12
29	22.4	>7000	12	5.5	45	7.5	48000	6.2
22	24	>7000	83	7	>200	11.5	56000	19.5

[a]  $E_{\max}^{\text{eff}}$  is the averaged value over the cathode size.

carried out to study the development of temperature and concentration profiles with ferrocene as a CVD precursor above and on the substrate surface. Our chemistry-based model for ferrocene decomposition and the reactions describing molecular weight growth consists of 2653 reactions among 299 species. The major gas-phase species were found to be H<sub>2</sub>, C<sub>10</sub>H<sub>8</sub>, C<sub>12</sub>H<sub>8</sub>, C<sub>6</sub>H<sub>6</sub>, and C<sub>2</sub>H<sub>4</sub>. Our modeling studies were supplemented by mass-spectroscopic in situ gas-phase analysis of the substrate boundary layer under real CVD reaction conditions resulting in the identification of reaction products as a function of temperature, which qualitatively agree with the predicted data. Large numbers of homogeneously distributed field emitters with low onset fields were found. This was attributed to the high stability of the unique CNT structure and the scattered, isolated CNT distribution on top of the substrate. In addition strong field enhancement and stable high current-carrying capability after dc processing over some hours were achieved on the new sample morphologies. A strong correlation between the average pore diameter on the alumina template and the current density of the CNTs was found. This supports the improved anchoring of the CNT structures on the alumina resulting in excellent FE performance. For an optimized sample of 24 mm<sup>2</sup>, resulting dc (pulsed) current densities up to 83 (200) mAcm<sup>-2</sup> at 7 (11) V $\mu\text{m}^{-1}$  have been achieved, which are close to the highest literature values.

## 4. Experimental Section

### 4.1. CVD Synthesis

Alumina membranes (Anopore) or homemade porous alumina<sup>[18,30]</sup> substrates were fixed perpendicular to the gas flow between two metallic rings fitted tightly into a quartz tube reactor with three individual heating zones.<sup>[30]</sup> Aluminum tris(*sec*-butoxide) (300 mg/1.22 mmol) was then introduced into the first heating

zone under argon while the membrane was located in the second heating zone. The furnace was heated to 823 K in the second and third heating zone while the first was adjusted to 623 K. During heating, a dynamic vacuum of 1 mbar was applied on the back side of the membrane. A small amount of residual organoaluminum precursor (decomposition) was removed after 3 h and 50 mg (0.27 mmol) of ferrocene was placed in the first heating zone. The first heating zone was maintained at 623 K the second and third were held at 1123 K. After complete sublimation the reactor was cooled to ambient conditions under argon.

### 4.2. Molecular-Beam-Coupled Quadrupole Mass Spectroscopy (MB-QMS)

To study the gas-phase chemistry during CVD-based nanotube synthesis, we employed in situ molecular-beam-coupled quadrupole mass spectroscopy (MB-QMS) (Figure 19),<sup>[39]</sup> which is a powerful analytical tool to detect stable and radical gas-phase species in combustion<sup>[46–50]</sup> or CVD processes.<sup>[51,52]</sup> Previously we successfully applied MB-QMS to diamond CVD<sup>[53]</sup> and MOCVD of GaN<sup>[54,55]</sup> and InN.<sup>[53]</sup>

Ferrocene was evaporated at 343–383 K and directed into the cylindrical (7.5 cm internal diameter) low-pressure titanium reaction chamber via a heated gas-transfer system with exit tem-

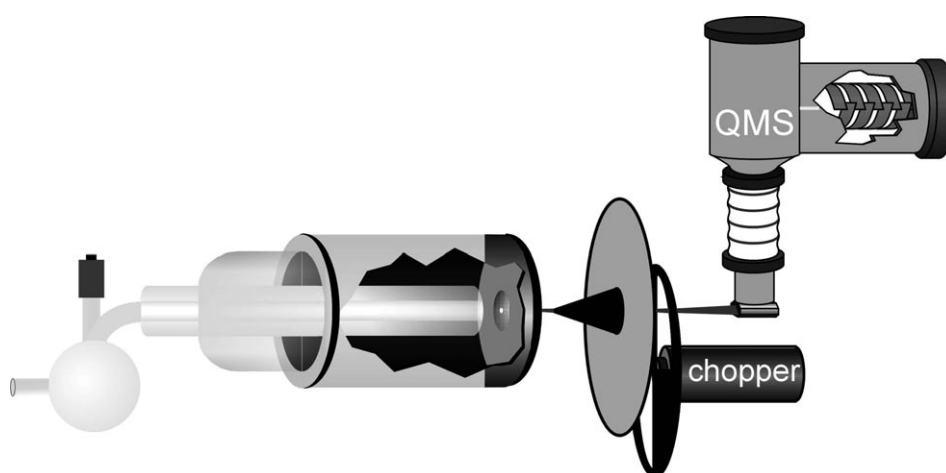


**Figure 19.** Schematic setup of the mass spectrometer used to analyze the boundary layer near the substrate during ferrocene CVD. From left to right: ferrocene vaporization, titanium reactor with heated sapphire substrate on the bottom, skimmer, chopper to modulate the reactor signal, and quadrupole mass spectrometer (QMS) to analyze the extracted gas sample.

peratures of 673 K (Figure 19). The precursor was injected onto the substrate (2.5-cm diameter) via a coaxial steel tube, separated 1 cm from the substrate surface. The substrate temperature was controlled by a thermocouple placed between the substrate and a boron nitride heating element attached to the reactor bottom. Gas was sampled at the substrate surface via a hole (100–300  $\mu\text{m}$  diameter) generated by laser ablation. Three-stage differential pumping reduced the pressure from a few mbar, to about  $10^{-4}$  mbar behind the orifice and  $10^{-7}$  mbar inside the analysis chamber. Here, the gas was ionized by a 10–70 eV crossbeam electron gun and analyzed by a QMS with single-ion detection. A chopper modulates the gas flow originating from the substrate thus minimizing background gas signals from the analysis chamber by computing the difference between open and closed chopper half-cycles. Mass spectra from 1–300 amu were captured with 0.4 amu resolution, sensitivities in the  $\mu\text{bar}$  range, and six orders of magnitude dynamic range.<sup>[53–56]</sup>

#### 4.3. FE Measurement System

Integral  $I$ - $V$  curves of FE cathodes were measured in diode configuration with online imaging of the current distribution at pressures of  $10^{-6}$  mbar.<sup>[40]</sup> The samples were fixed on Al cathodes by means of Leit-Tabs (Plano) and assembled parallel to the phosphor anodes (tilt 10  $\mu\text{m}$ ). The electrode spacing was adjusted between 125 and 400  $\mu\text{m}$ . Currents up to 50 mA and dc voltages up to 5 kV were applied by a power supply (FUG) partially with current-controlled PID voltage regulation or remote-controlled pulsed operation (2 ms full-height rise time). The average current was measured with an analog (Keithley 610C) or digital pico-ammeter (Keithley 6485E) and scaled with the duty cycle in case of pulsed operation.<sup>[41]</sup> The luminescent screen images were taken by a CCD camera either as single shots ( $1600 \times 1200$  pixels  $\rightarrow$  20  $\mu\text{m}$ ) or online ( $768 \times 576$  pixels) transferred via video recorder and frame grabber (Matrox meteor II) to a computer (Pentium III). Real-time data saving and processing was performed with a frequency of 10 Hz by means of AnalySIS software. A quadrupole mass spectrometer (QMG 112) served as an indicator for luminescent layer evaporation with a partial pressure sensitivity of  $5 \times 10^{-11}$  mbar (e.g., for S and C).

A field-emission scanning microscope was used for the localization and investigation of field emitters at a base pressure of  $10^{-7}$  Pa.<sup>[40]</sup> The scans of the CNT samples were performed with W tip anodes of 10–30  $\mu\text{m}$  diameter at about the same distance to the cathodes. The resulting electric field on the samples ( $E = U/ad$ ) is reduced by a correction factor  $a > 1$ , which has been calculated with the numerical code MAFIA.<sup>[57]</sup> The spacing between the anode and the sample was adjusted by means of 3D stepper-motor-driven sliding tables and a 3D piezo translator below the tiltable sample holder ( $\Delta z$  accuracy of  $\pm 1 \mu\text{m}$  over a  $1 \text{ cm}^2$  scan area) and monitored with a long-distance optical microscope (Questar) and a CCD camera.

#### Acknowledgements

We cordially acknowledge financial support by the Volkswagen Foundation, Hannover, Germany, through the funding initiative "Complex Materials".

- [1] W. A. de Heer, A. Chatelain, D. Ugarte, *Science* **1995**, *270*, 1179–1180.
- [2] S. S. Fan, M. G. Chapline, N. R. Franklin, T. W. Tomblor, A. M. Cassell, H. Dai, *Science* **1999**, *283*, 512–514.
- [3] N. S. Xu, S. Ejaz Huq, *Mater. Sci. Eng. R* **2005**, *48*, 47–189.
- [4] W. I. Milne, K. B. K. Teo, G. A. J. Amaratunga, P. Legagneux, L. Gangloff, J. P. Schnell, V. Semet, V. Thien Binh, O. Groening, *J. Mater. Chem.* **2004**, *14*, 933–943.
- [5] K. A. Dean, T. P. Burgin, B. R. Chalamala, *Appl. Phys. Lett.* **2001**, *79*, 1873–1875.
- [6] V. Semet, V. T. Binh, P. Vincent, D. Guillot, K. B. K. Teo, M. Chhowalla, G. A. J. Amaratunga, W. I. Milne, P. Legagneux, D. Pribat, *Appl. Phys. Lett.* **2002**, *81*, 343–345.
- [7] W. K. Yi, T. W. Jeong, S. G. Yu, J. N. Heo, C. S. Lee, J. H. Lee, W. S. Kim, J. B. Yoo, J. M. Kim, *Adv. Mater.* **2002**, *14*, 1464–1468.
- [8] G. Z. Yue, Q. Qiu, B. Gao, Y. Cheng, J. Zhang, H. Shimoda, S. Chang, J. P. Lu, O. Zhou, *Appl. Phys. Lett.* **2002**, *81*, 355–357.
- [9] C. Bower, W. Zhu, D. Shalom, D. Lopez, L. H. Chen, P. L. Gammel, S. Jin, *Appl. Phys. Lett.* **2002**, *80*, 3820–3822.
- [10] L. Nilsson, O. Groening, C. Emmenegger, O. Kuettel, E. Schaller, L. Schlapbach, H. Kind, J.-M. Bonard, K. Kern, *Appl. Phys. Lett.* **2000**, *76*, 2071–2073.
- [11] a) C. Klinke, R. Kurth, J. M. Bonard, K. Kern, *J. Phys. Chem. B* **2002**, *106*, 11191–11195; b) G. Gu, G. Philipp, X. Wu, M. Burghard, A. M. Bittner, S. Roth, *Adv. Funct. Mater.* **2001**, *11*, 295–298.
- [12] J. Dijon, C. Bridoux, A. Fournier, F. Geffraye, T. Goislart de Monsabert, B. Montmayeul, M. Levis, D. Sarrasin, R. Meyer, K. A. Dean, B. F. Coll, S. Johnson, C. Hagen, J. Jaskie, *J. S. I. Displays* **2004**, *12*, 373–378.
- [13] H. M. Manohara, M. J. Bronikowski, M. Hoenk, B. D. Hunt, P. H. Siegel, *J. Vac. Sci. Technol. B* **2005**, *23*, 157–161.
- [14] C. J. Lee, D. W. Kim, T. J. Lee, Y. C. Choi, Y. S. Park, Y. H. Lee, W. B. Choi, N. S. Lee, G. S. Park, J. M. Kim, *Chem. Phys. Lett.* **1999**, *312*, 461–468.
- [15] C. N. R. Rao, A. Govindaraj, *Acc. Chem. Res.* **2002**, *35*, 998–1007, and references therein.
- [16] C. N. R. Rao, B. Satishkumar, A. Govindaraj, M. Nath, *ChemPhys-Chem* **2001**, *2*, 78–105.
- [17] G. L. Hornyak, A. C. Dillon, P. A. Parilla, J. J. Schneider, N. Czap, K. M. Jones, F. S. Fasoan, A. Mason, M. J. Heben, *Nanostruct. Mater.* **1999**, *12*, 83–88.
- [18] J. J. Schneider, J. Engstler, *Eur. J. Inorg. Chem.* **2006**, *9*, 1723–1736.
- [19] Z. F. Ren, Z. P. Huang, J. W. Xu, J. H. Wang, P. Bush, M. P. Siegal, P. N. Provencio, *Science* **1998**, *282*, 1105–1107.
- [20] L. C. Qin, D. Zhou, A. R. Krauss, D. M. Gruen, *Appl. Phys. Lett.* **1998**, *72*, 3437–3439.
- [21] R. S. Wagner, W. C. Ellis, *Appl. Phys. Lett.* **1964**, *4*, 89–90.
- [22] H. Dai, A. G. Rinzler, P. Nikolaev, A. Thess, D. T. Colbert, R. E. Smalley, *Chem. Phys. Lett.* **1996**, *260*, 471–475.
- [23] C. J. Lee, S. C. Lyu, H.-W. Kim, C.-Y. Park, C.-W. Yang, *Chem. Phys. Lett.* **2002**, *359*, 109–114.
- [24] S. M. Huang, A. W. H. Mau, *J. Phys. Chem. B* **2003**, *107*, 3455–3458.
- [25] C. Klinke, E. Delvigne, J. V. Barth, K. Kern, *J. Phys. Chem. B* **2005**, *109*, 21677–21680.
- [26] Y. Li, W. Kim, Y. Zhang, M. Rolandi, D. Wang, H. Dai, *J. Phys. Chem. B* **2001**, *105*, 11424–11431.

- [27] B. Günther, A. Göhl, G. Müller, J. Engstler, J. J. Schneider, *Proc. 13th Int. Vacuum Microelectronics Conf., Davis, CA*, **2001**, pp. 207–208.
- [28] B. Günther, Dissertation, Univ. of Wuppertal, **2002**, WUB-DIS 2002-8.
- [29] D. Lysenkov, H. Abbas, G. Müller, J. Engstler, K. P. Budna, J. J. Schneider, *J. Vac. Sci. Technol. B* **2005**, *23*, 809–813.
- [30] J. J. Schneider, J. Engstler, K. P. Budna, C. Teichert, S. Franzka, *Eur. J. Inorg. Chem.* **2005**, *12*, 2352–2359.
- [31] Fluent user manual Version 6.1. Fluent Inc., Lebanon, NH.
- [32] a) O. Deutschmann, S. Tischer, C. Correa, D. Chatterjee, S. Kleitzsch, V. M. Janardhanan, DETCHEM software package, 2.0 ed., www.detchem.com, Karlsruhe, **2004**; b) S. Tischer, O. Deutschmann, *Catal. Today* **2005**, *105*, 407–413.
- [33] T. Hirasawa, C. Sung, Z. Yang, A. Joshi, H. Wang, *Combust. Flame* **2004**, *288*–299.
- [34] C. Sheng, A. M. Dean, *J. Phys. Chem. A* **2004**, *108*, 3772–3783.
- [35] J. Müller, L. D'Or, *J. Organomet. Chem.* **1967**, *10*, 313–322.
- [36] W. Gurlit, R. Zimmermann, C. Giesemann, T. Fernholz, J. Wolfrum, U. Platt, J. P. Burrows, V. Ebert, *Appl. Opt.* **2005**, *44*, 91–102.
- [37] V. Ebert, T. Fernholz, C. Giesemann, H. Pitz, H. Teichert, J. Wolfrum, H. Jaritz, *Proc. Combust. Inst.* **2000**, *28*, 423–430.
- [38] L. Ma, S. T. Sanders, J. B. Jeffries, R. K. Hanson, *Proc. Combust. Inst.* **2002**, *29*, 161–166.
- [39] J. C. Biordi, *Prog. Energy Combust. Sci.* **1977**, *3*, 151–173.
- [40] D. Lysenkov, G. Müller, *Int. J. Nanotechnol.* **2005**, *2*, 239–254.
- [41] D. Lysenkov, Dissertation, Univ. of Wuppertal, WUB-DIS 2006-2, **2006**.
- [42] O. Gröning, L. O. Nilsson, P. Gröning, L. Schlapbach, *Solid State Electron.* **2001**, *45*, 929–944.
- [43] L. Nilsson, O. Groening, P. Groening, O. Kuettel, L. Schlapbach, *J. Appl. Phys.* **2001**, *90*, 768–780.
- [44] D. Lysenkov, G. Müller, *J. Vac. Sci. Technol. B* **2006**, *24*, 1067–1071.
- [45] D. Lysenkov, A. Dangwal, G. Müller, J. Engstler J. J. Schneider, *Proc. 19th Int. Vacuum Nanoelectronic Conf., Guilin, July* **2006**, pp. 225–226.
- [46] K. Kohse-Höinghaus, *Isr. J. Chem.* **1999**, *39*, 25–39.
- [47] G. We, A. T. Hartlieb, J. Brand, B. Atakan, H. Kohse, *Combust. Flame* **1999**, *118*, 37–50.
- [48] K. Kohse-Höinghaus, A. Schocker, T. Kasper, M. Kamphus, A. Brockhinke, *Z. Phys. Chem.* **2005**, *219*, 583–599.
- [49] F. Qi, A. McIlroy, *Combust. Sci. Technol.* **2005**, *177*, 2021–2037.
- [50] S. McEnally, L. D. Pfefferle, B. Atakan, K. Kohse-Höinghaus, *Prog. Energy Combust. Sci.* **2006**, *32*, 247–294.
- [51] T. Haase, K. Kohse-Höinghaus, B. Atakan, H. Schmidt, H. Lang, *Chem. Vap. Deposition* **2003**, *9*, 144–148.
- [52] U. Bergmann, V. Reimer, B. Atakan, *Phys. Status Solidi A* **1999**, *176*, 719–722.
- [53] V. Zumbach, J. Schäfer, J. Tobai, M. Ridder, T. Dreier, T. Schaich, J. Wolfrum, B. Ruf, F. Behrendt, O. Deutschman, J. Warnatz, *J. Chem. Phys.* **1997**, *107*, 5918–5928.
- [54] J. Schäfer, J. Wolfrum, R. A. Fischer, H. Sussek, *Chem. Phys. Lett.* **1999**, *300*, 152–156.
- [55] J. Schäfer, A. Simons, J. Wolfrum, R. A. Fischer, *Chem. Phys. Lett.* **2000**, *319*, 477–481.
- [56] J. Schäfer, J. Wolfrum, R. A. Fischer, H. Sussek, *Chem. Vap. Deposition* **1999**, *5*, 205–207.
- [57] T. Habermann, Dissertation, Univ. of Wuppertal, WUB-DIS 98-18, **1999**.

Received: October 25, 2006  
Revised: January 29, 2007